

REPORT DOCUMENTATION PAC

AFRL-SR-BL-TR-98-

0188

0711

ing data sources,
her aspect of this
ts, 1215 Jefferson
503.

Public reporting burden for this collection of information is estimated to average 1 hour per resp gathering and maintaining the data needed, and completing and reviewing the collection of infor collection of information, including suggestions for reducing this burden, to Washington Headqu Davis Highway, Suite 1204, Arlington, VA 22202-4302, and to the Office of Management and Bud

1. AGENCY USE ONLY (Leave blank)		2. REPORT DATE	3. REPORT TYPE AND DATES COVERED	
		October 1998	Final Technical: 01 MAY 97 to 31 JUL 98	
4. TITLE AND SUBTITLE			5. FUNDING NUMBERS	
Research on High Resolution Imaging and Fiber Optical Networks			G F49620-97-1-0349 PR 2301/AS FQ8671-9701302	
6. AUTHOR(S)				
Dr. James F. Young Professor, Electrical & Computer Engineering				
7. PERFORMING ORGANIZATION NAME(S) AND ADDRESS(ES)			8. PERFORMING ORGANIZATION REPORT NUMBER	
Rice University Office of Sponsored Research P.O. Box 2692 Houston, TX 77252				
9. SPONSORING / MONITORING AGENCY NAME(S) AND ADDRESS(ES)			10. SPONSORING / MONITORING AGENCY REPORT NUMBER	
AFOSR/NE Dr. Howard R. Schlossberg 110 Duncan Avenue Suite B115 Bolling AFB, DC 20332-0001				
11. SUPPLEMENTARY NOTES				
12a. DISTRIBUTION / AVAILABILITY STATEMENT DISTRIBUTION STATEMENT: Approved for public release Distribution Unlimited			12b. DISTRIBUTION CODE	
13. ABSTRACT (Maximum 200 words)				
<p>The purpose of this grant was to provide support to allow a student working under the preceding grant, F49620-94-1-0017 to transition to new funding and to finish his graduate degree. Both objectives were met. The research program involved two projects. The first focused on the development of extreme ultraviolet (XUV) sources, and their application to the development of high resolution, microscopic imaging techniques. That project came to close shortly after the beginning of this grant. The second project investigated unique approaches to building multiuser optical fiber networks.</p>				
14. SUBJECT TERMS Lasers; Ultraviolet; Vacuum Ultraviolet, XUV, VUV, Fiber Optics.			15. NUMBER OF PAGES 4 plus attach.	
			16. PRICE CODE	
17. SECURITY CLASSIFICATION OF REPORT UNCLASSIFIED	18. SECURITY CLASSIFICATION OF THIS PAGE UNCLASSIFIED	19. SECURITY CLASSIFICATION OF ABSTRACT UNCLASSIFIED	20. LIMITATION OF ABSTRACT	

Research on High Resolution Imaging and Fiber Optical Networks

AFOSR GRANT F49620-97-1-00349
FINAL TECHNICAL REPORT

James. F. Young
Principal Investigator & Professor

Department of Electrical and Computer Engineering,
Rice University, P.O. Box 1892, Houston, TX 77251
Phone: (713) 527-4721; FAX: (713) 524-5237; young@rice.edu

01 May 1997 — 31 July 1998

1 Introduction

The purpose of this grant was to provide support to allow a student working under the preceding grant, F49620-94-1-0017 to transition to new funding and to finish his graduate degree. Both objectives were met. The research program involved two projects. The first focused on the development of extreme ultraviolet (XUV) sources, and their application to the development of high resolution, microscopic imaging techniques. That project came to close shortly after the beginning of this grant. The second project investigated unique approaches to building multiuser optical fiber networks.

2 Personnel Supported This Period

Senior Personnel

James F. Young, Principle Investigator and Professor.

Students

Tasshi Dennis, graduate student; Ph.D. completed September 1998.

Honors

Tasshi Dennis was awarded a National Research Council two year Research Associate Fellowship at NIST, Optoelectronics Division, Fiber and Discrete Components Group, Boulder, CO.

3 Summary of Research

3.1 Short Wavelength Imaging

This grant provided supplemental and continuing student support for the preceding grant, F49620-94-1-0017, which ended 14 October 1997. The short wavelength imaging project was terminated at that time because of technical and funding reasons. Consequently, all effort on this grant in that area has been joint with F49620-94-1-0017, and the reader is referred to its Final Technical Report for details. The final publication in the area is listed below, and attached to this report.

3.2 Fiber Optic Networks

The bulk of the effort supported by this grant focused on multi-user, multi-wavelength optical fiber communications systems. Wavelength division multiplexing (WDM) is a very successful technique for increasing the capacity of point-to-point fiberoptic communications links. We have been investigating more sophisticated encoding techniques that promise even further increases in functionality, particularly for multiuser networks. For example, radio frequency (RF) code division multiple access (CDMA) has been very successful at supporting a large pool of asynchronous network subscribers sharing a common channel, increasing noise tolerance, and providing user security and flexibility. This success has been primarily due to the development and use of bipolar, $\{+1, -1\}$, code sequences and bipolar correlation detection. While both time and spectral domain optical CDMA have been studied, the results to date have been poor because direct detection optical channels are inherently unipolar, $\{+1, 0\}$, and cannot directly implement the RF bipolar coding and correlation detection.

We have invented a technique to achieve true bipolar encoding and decoding for optical spectral CDMA [“All-Optical CDMA with Bipolar Codes,” L. Nguyen, B. Aazhang, and J. F. Young, *Electronics Letters* **31**, 469–470 (1995); U.S. Patent No. 5,760,941], and performed proof-of-principle measurements. We have examined the practical implementation of passive, all-optical encoders and decoders incorporating these principles, using a fiber-based, three user testbed capable of OC-24 (1.25 Gb/s) operation, and developed a numerical simulation of the encoder and decoder correlation process to study the various optical effects that influence the detection performance. Recently, we have completed bit error rate measurements under a variety of conditions using our testbed. Details of this work can be found in the papers listed in the next section.

Our work has shown that passive, all-optical correlators are attractive for high-speed network applications where asynchronous operation and independence of data rate are desired. They are able to process the extremely high combined data rate on a common network channel while the detection electronics operate at only individual user rates. However, optical distortions cause degradation of correlator performance and have a direct impact on the capacity of a network to support simultaneously active users. Our numerical simulations, analytical results, and experimental measurements have identified wavelength scale distortion as a critical optical parameter in the correlation process and illustrated the importance of well-matched physical characteristics when using multiple gratings or other dispersive elements. Based on our results, we have received a grant to continue the work from the Texas Advanced Technology Program.

The usefulness of our technique relative to WDM will ultimately depend on a tradeoff between the added complexity and the added functionality. Encoder and correlator designs that minimize complexity and optical distortions are thus very important. We have begun a collaboration with Dr. Ray Chen at the University of Maryland, Baltimore County, to design and fabricate planar waveguide integrated optical circuits that will implement our encoder and correlator concepts on a single photonic chip. These devices will improve performance while minimizing complexity and cost.

4 Publications and Presentations of Supported Work

“Measurements of BER Performance for Bipolar Encoding of an SFS,” T. Dennis and J. F. Young, (In preparation).

“Optical Implementation of Bipolar Codes,” T. Dennis and J. F. Young, (In Review; draft attached).

“Experimental Demonstration of All-Optical CDMA using Bipolar Codes,” Tasshi Dennis, Ph.D. Dissertation, Electrical and Computer Engineering Department, Rice University, Houston, Texas (September 1998).

“Experimental Demonstration of Bipolar Codes for Optical Spectral Amplitude CDMA Communication,” L. Nguyen, T. Dennis, B. Aazhang, and J. F. Young, *J. Lightwave Technology* **15**, 1647–1653 (1997).

“Laser-Produced Plasmas as Short Wavelength, Incoherent Optical Sources,” J. F. Young, in *Atomic, Molecular, and Optical Physics: Electromagnetic Radiation*, F. B. Dunning and R. G. Hulet, eds., , Chapter 1 (Academic Press, 1997).

“Imaging Characteristics of Poly(methyl methacrylate) at Vacuum Ultraviolet Wavelengths,” I. E. Ferincz, C. Tóth, and J. F. Young, *J. Vac. Sci. Technol. B* **15**, 828–832 (1997) (Attached).

"All-Optical Encoders and Decoders for Spectral CDMA using Bipolar Codes," T. Dennis and J. F. Young; in *All-Optical Networking: Architecture, Control, and Management Issues*, SPIE (in press).

"Wavelength Encoding for Optical Networks," T. Dennis and J. F. Young; Int. Conf. on Applications of Photonic Technology, Ottawa, Canada, July 1998 (Invited).

"Wavelength Encoding to Reduce Four-Wave Mixing Crosstalk in Multi-Wavelength Channels," Y. Guo, B. Aazhang, and J. F. Young; IEEE Lasers and Electro-Optics Society Annual Meeting, San Francisco, CA, November 1997.

"Demonstration of All-Optical CDMA with Bipolar Codes," T. Dennis, B. Aazhang, and J. F. Young; IEEE Lasers and Electro-Optics Society Annual Meeting, San Francisco, CA, November 1997.

5 Relationship to Other Programs and Support

The imaging applications portion of this work was jointly supported by the National Science Foundation; the optical communications work was jointly supported by the Texas Advanced Technology Program.

Optical Implementation of Bipolar Codes *

Tasshi Dennis and James F. Young (*Fellow, IEEE*)

Department of Electrical and Computer Engineering,
Rice University, MS-366, PO Box 1892, Houston, TX 77251
Phone: 713-527-4721; FAX: 713-524-5237; young@rice.edu

Abstract

The physical implementation of a bipolar encoding scheme suitable for fiber optic networks is reported with both experimental and theoretical results. The power spectrum of an erbium-doped superfluorescent fiber source is encoded, the bipolar correlations of the codes are verified and rejection of multiple-access interference is demonstrated in a fiber-based testbed. Simulations of the correlation process identify key optical parameters and physical characteristics important to the design of future systems. A modification to the experimental testbed, made according to the theoretical analysis, results in improved correlation performance.

1 Introduction

Wavelength division multiplexing (WDM) is a very successful technique for increasing the capacity of fiberoptic communications links. WDM is the simplest form of wavelength encoding, and we have been investigating more sophisticated encoding techniques that promise even further increases in functionality, particularly for multiuser networks. For example, radio frequency (RF) code division multiple access (CDMA) has been very successful at supporting a large pool of asynchronous network subscribers sharing a common channel, increasing noise tolerance, and providing user security and flexibility. This success has been primarily due to the development and use of bipolar, $\{+1, -1\}$, code sequences and bipolar correlation detection. While both time and spectral domain optical CDMA have been studied [1, 2, 3], the results to date have been poor because direct detection optical channels are inherently unipolar, $\{+1, 0\}$, and cannot directly implement the RF bipolar coding and correlation detection.

We have previously reported a technique to achieve true bipolar encoding and decoding for optical spectral CDMA [4], and presented proof-of-principle measurements [5]. In this

*This work was jointly supported by the Texas Advanced Technology Program and the U.S. Air Force Office of Scientific Research.

paper, we examine the practical implementation of passive, all-optical encoders and decoders incorporating these principles. First, we present experimental results using a fiber-based, three user testbed capable of OC-24 (1.25 Gb/s) operation. Second, we develop a numerical simulation of the encoder and decoder correlation process to study the various optical effects that influence the detection performance. Finally, we make modifications to our decoder based on our theoretical results and show an improvement in correlation performance.

2 Encoder and Decoder Operation

Our basic scheme has been reported previously [4, 5], and is based on representing a bipolar code as two unipolar codes. For each length- N bipolar code X , we form a unipolar sequence U by replacing each -1 with 0 . The unipolar super-code J of length $2N$ is then formed as the concatenation of U and its complement, $U \oplus \bar{U}$. At the decoder, this technique reduces the bipolar correlation to two unipolar correlations that can be performed using a passive optical system and intensity detection. Our experimental apparatus performs spectral encoding and decoding of a superfluorescent fiber source (SFS) using a bulk grating and amplitude mask as shown in Fig. 1. Shown in Fig. 2 is the fiber-based testbed constructed for this

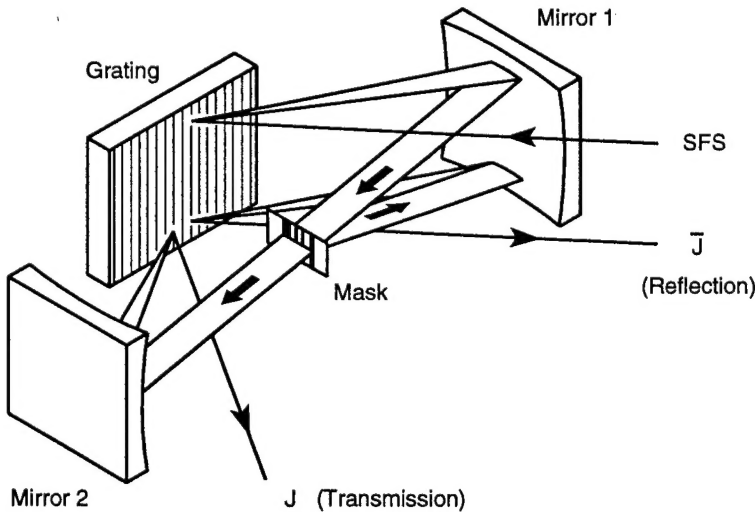


Figure 1: The geometry for the grating based encoders. The spectral patterns of the two outputs, J and \bar{J} are complements of one another, and are used to transmit a One and Zero respectively. The decoder has exactly the same geometry, but the SFS input is replaced by the signal from the network channel, and the outputs are focused onto a balanced receiver.

series of measurements. We used a SFS consisting of 40 m of highly doped erbium fiber pumped by a 150 mW, 980 nm pigtailed diode. About 22 mW of randomly polarized SFS power was divided with a fiber polarization splitter, forming broadband light sources for two encoders. We encoded about 9 nm of the bandwidth centered around the 1530 nm peak using Walsh codes. These codes, which have zero crosscorrelations in theory, were used to simplify comparison between theory and experimental results. Three super-codes of length

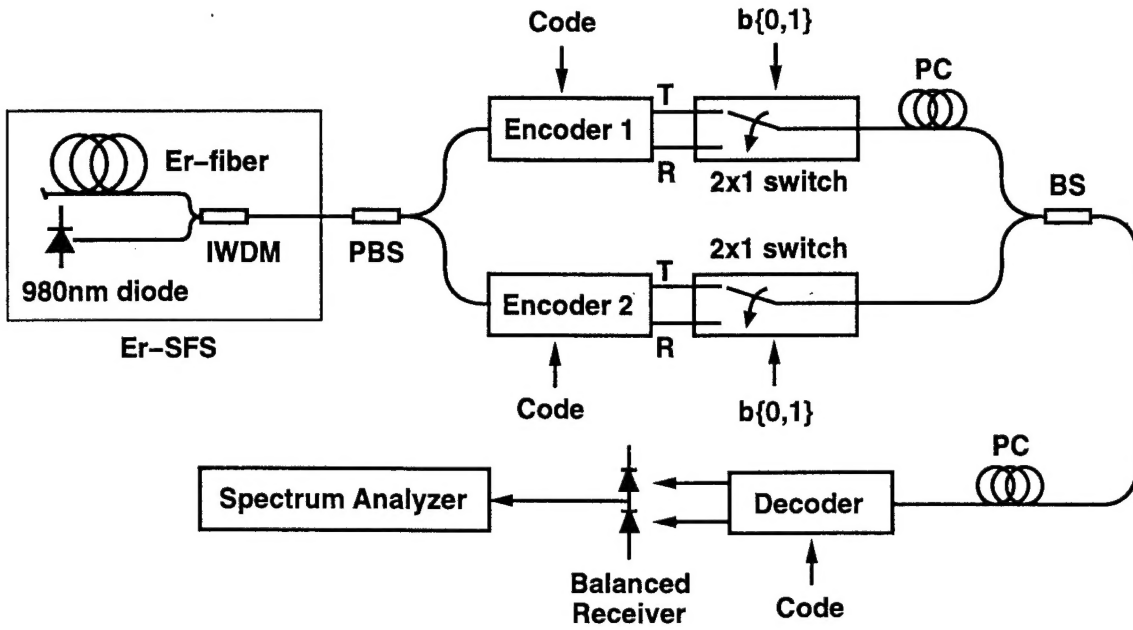


Figure 2: Experimental setup of the spectral amplitude CDMA testbed; showing superfluorescent fiber source SFS, isolator/wavelength division multiplexer IWDM, fiber splitters and combiners BS and PBS, polarization controllers PC, and reflection and transmission outputs R and T.

32, which we shall denote as J_A , J_B , J_C , and their complements, were etched on aluminum-coated glass substrates for each encoder and decoder in the testbed. The smallest etched feature was $200\ \mu\text{m}$ wide, corresponding to a spectral slice of approximately $0.18\ \text{nm}$ of optical bandwidth. To simplify mask fabrication, guardbands between adjacent code elements were not used. The two outputs of each encoder, formed according to the selected bipolar code, are ON/OFF modulated with 2×1 interferometric 1 GHz optical switches according to the information symbol b . The modulated outputs are combined to form the network channel and sent to the decoder. The mask of the decoder performs the bipolar correlation according to the code selected for receiving, and the output is detected with a balanced receiver and monitored with a spectrum analyzer.

3 Correlation Measurements

The correlations between the codes were measured with a single encoder and decoder. With the decoder adjusted to receive a particular code, the encoder mask was positioned in successive measurements to transmit any one of the available code patterns. This procedure was repeated for each of the codes at the decoder, while the optical switch was driven by a sinusoid. As shown in Fig. 3, for the same code (J_A , J_B , J_C) at encoder and decoder a large autocorrelation power was detected, one each for positive and negative receiver currents. For mismatched codes, the crosscorrelation signals were on average $23.2\ \text{dB}$ below the autocorrelations, showing that a binary information symbol can be recovered by a zero threshold

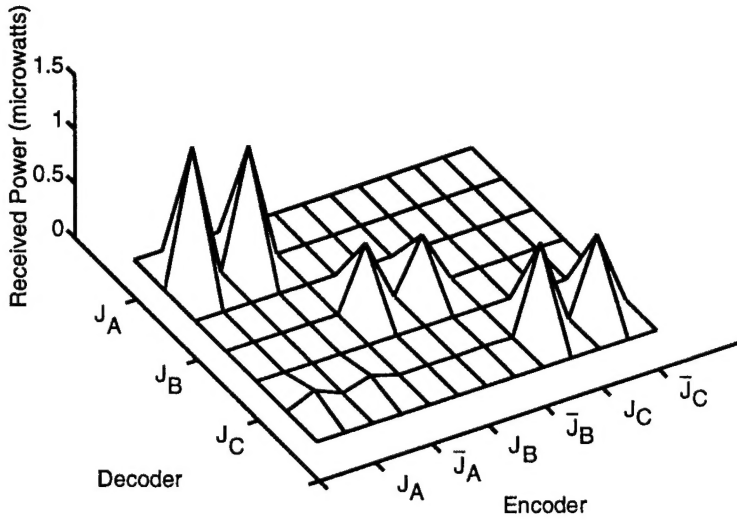


Figure 3: Correlations of the codes measured on the spectrum analyzer. For mismatched codes, the crosscorrelation signals are an average 23.2 dB below the autocorrelations

operation. The non-zero crosscorrelations and the variation of the autocorrelations are believed to be due to a combination of mask fabrication tolerances and the optical properties of the system, which are discussed in the next section.

The multiple access interference (MAI) rejection was evaluated using two encoders and one decoder. While one encoder and decoder were adjusted to matched codes, the second encoder sent the other codes as interference in successive measurements. Figure 4 summarizes the MAI measurements, showing the change in signals measured at the decoder when the interference signal was present. To confirm that the observed rejection was not simply frequency multiplexing, MAI measurements were performed with the encoders driven at the same and at different modulation frequencies. In both cases the conclusion was the same: the degradation of the desired signal was less than 1.7 dB, and the decoder could reject MAI.

4 Simulation Results

Despite the ideal orthogonality of Walsh codes, our experimental results do not show zero crosscorrelations or complete interference rejection. We believe this nonideal behavior is largely the result of optical effects occurring in the encoder and decoder. In previous work [5], we reported the measurement of wavelength scale distortion and limited resolution. Each of these effects is apparent from the measured spectra of Fig. 5, which shows the 1530 nm spectral peak of the erbium-doped SFS, an amplitude mask pattern, and the resulting encoded spectrum seen at the decoder mask. The encoded pattern is about 5% wider ($500 \mu\text{m}$ over a 10 mm spatial field) than the encoding mask. The rounded chip shapes indicate a full-width-at-half-maximum resolution of $175 \mu\text{m}$. Accurate correlations also require that

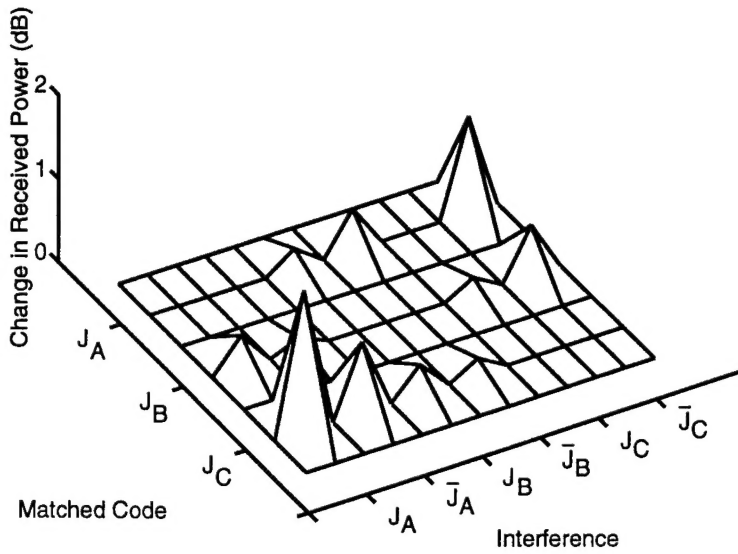


Figure 4: The change in signals measured at the decoder when an interference signal is present.

each code chip have equal power, and the bar-widths of the masks were intentionally varied to compensate for the nonuniform spectral power density of the SFS. This compensation is an approximation and the inaccuracies degrade correlation performance.

To better understand the influence that all these optical parameters have on correlation performance, a numerical simulation was performed using the calculation tool Matlab. Using a signal processing approach, the optical processes were implemented independently, from the formation of the super-codes, to the detection of the correlation signals with a balanced receiver. The result of simulating the encoding of supercode J_C with the measured values of the optical parameters is shown in Fig. 6, which compares favorably with the measured spectrum of Fig. 5. Of the optical parameters considered, it would be useful to know which has the greatest impact on the correlation process, so that future systems, either ones incorporating new technology or modified versions of the existing one, can yield the greatest improvement in correlation performance. Shown in Fig. 7 (a) is the simulated autocorrelation signal as a function of the wavelength scale distortion for code J_B . At zero distortion, the autocorrelation is reduced to 58% of its optimal value by reduced chip contrast due to limited resolution. For an increasing magnitude of distortion, the autocorrelation signal is reduced further, with a slightly larger reduction for negative distortion because the total encoded power is also being reduced, while for positive distortion the power is being held constant by the spatial width of the decoder mask. Plot (b) shows the dependency of the crosscorrelation signal between decoder mask J_B and encoded pattern J_A , which predictably gets worse as the magnitude of the distortion increases. Plot (c) shows the ratio of the crosscorrelation curve (b) to the autocorrelation curve (a), which gives a signal-to-interference ratio (SIR), expressed as a percentage. At zero distortion, the SIR is 4.9% or -26.2 dB , due to the combined effects of limited resolution and imperfect compensation for the nonuniform

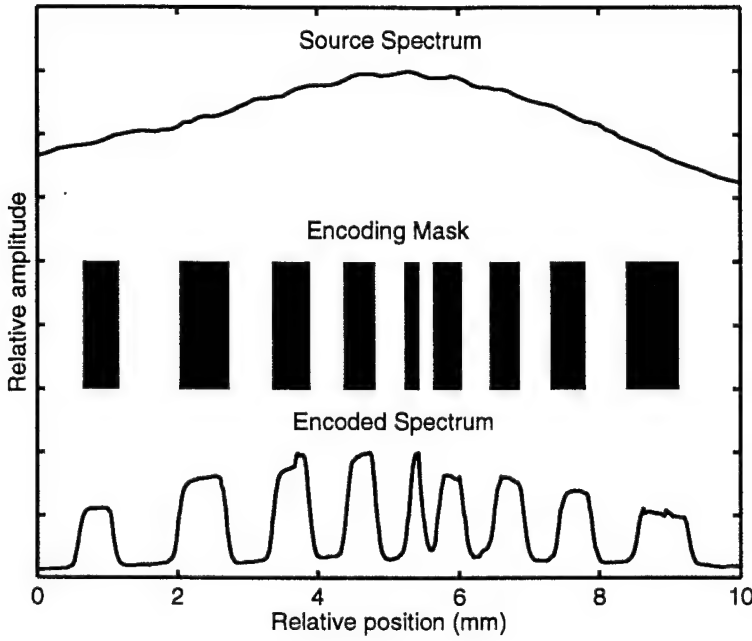


Figure 5: Erbium SFS spectrum, encoding mask, and an encoded spectrum as seen at the decoder mask. The pattern is super-code $J_C = (1001100110011001 \oplus 0110011001100110)$ used in the correlation measurements.

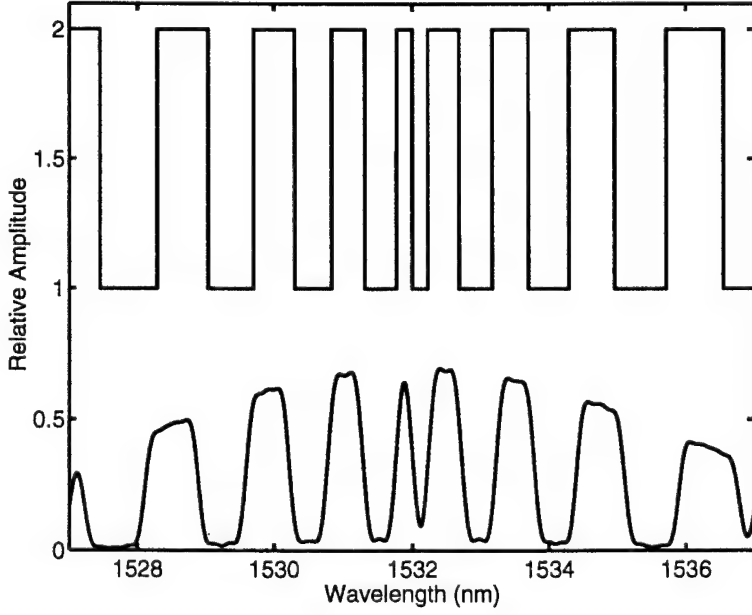


Figure 6: Simulation of the encoding process based on experimentally measured optical parameters, showing an encoding mask and a processed spectrum. The results resemble the measurements of Fig. 5.

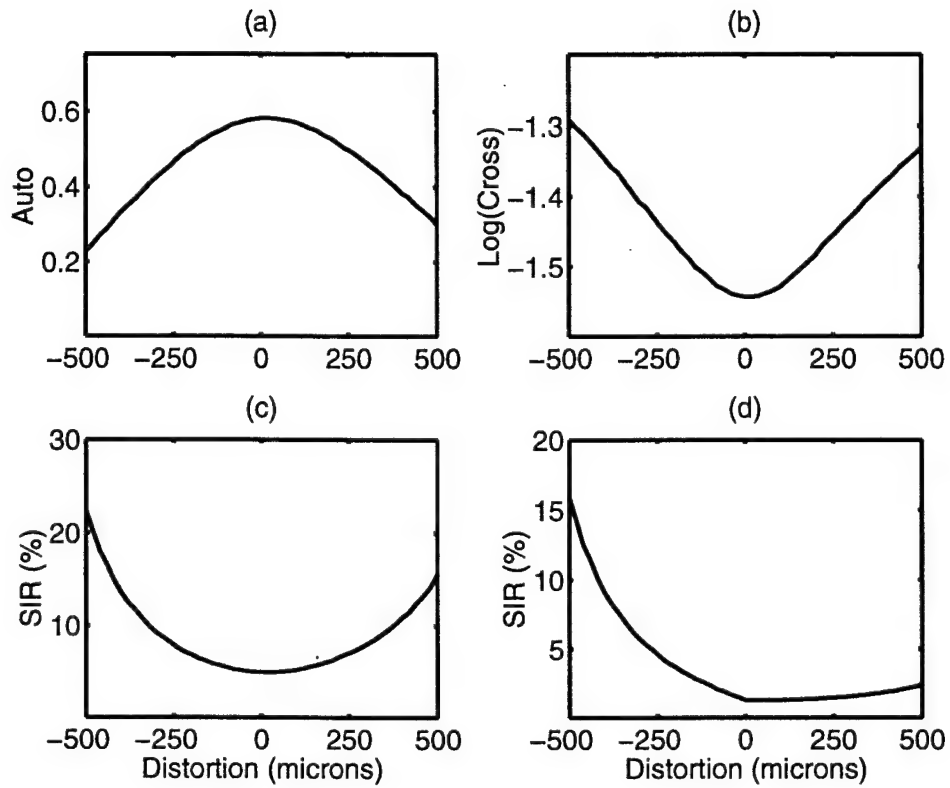


Figure 7: Simulated correlation performance as a function of the wavelength scale distortion. Plots (a), (b), and (c) were calculated for a decoder mask of J_B with spectra of J_A and J_B , and plot (d) was for a decoder mask of J_B and spectra of J_B and J_C .

spectral shape. At the experimental value of $+500 \mu\text{m}$ of distortion, the simulated SIR rises substantially to 15.6% or -16.1 dB , clearly demonstrating the devastating impact of this parameter. For comparison, the measured SIR for decoder mask J_B and encoder mask J_A from Fig. 3 was 6.5% or -23.7 dB . The measurements are better than the simulation results because of the ambiguity in horizontally positioning the decoder mask relative to the mask at the encoder. For the autocorrelation measurements, the correct horizontal position was easily found by maximizing the received signal. For the crosscorrelations, the ideal position should be where the received signal is minimum. However, horizontal positioning during a crosscorrelation measurement can also compensate for the signal imbalance that occurs from optical effects such as distortion and limited resolution, or even mask inaccuracies and defects, such as pin-holes. A number of alignment features on the masks help to minimize this problem, but the vertical translation of the masks required to change the codes adds variation to an already sensitive alignment.

Simulations with other codes at encoder and decoder revealed that the impact of the wavelength scale distortion is also code-dependent, as shown in Fig. 7 (d). The SIR curve shown is for a decoder mask of J_B and spectra of J_B and J_C . The gradually increasing SIR for positive distortion results from the decreasing autocorrelation signal shown in plot (a), while the crosscorrelation remains constant. Encoded spectral patterns for which the outermost features at long and short wavelengths are complementary do not cause an imbalance at the receiver for positive distortion.

While it might have been expected that limited resolution would be the critical parameter, the reduction in contrast between adjacent spectral chips does not degrade the balance of the photodiodes. Equal amounts of light are directed to the wrong detector, and the crosscorrelation signal remains zero. However, the limited resolution does degrade the magnitude of the autocorrelation signal, since light diffracted into neighboring spectral chips will be received by the wrong photodiode and subtracted from the desired signal of the other photodiode. This effect is apparent in the measurements of Fig. 3, where the autocorrelation peaks for code J_B are roughly half those for codes J_A and J_C . Although each of the super-codes is length 32, the code sequence for J_B is composed primarily of alternating 1's and 0's, while the sequences for J_A and J_C are composed primarily of repeated segments (11 and 00), reducing the effects of limited resolution.

To better understand the origin of the wavelength scale distortion of the decoder, an analytical sensitivity analysis was performed using the plate factor of the decoder. The plate factor P expresses the number of nanometers of optical bandwidth per millimeter of spatial extent in the mask plane. For a grating with a groove spacing of d , a collimation mirror of focal length f , and an observation wavelength λ at a dispersion angle of β ,

$$P = \frac{d \cos \beta}{f}. \quad (1)$$

A simple derivative of this expression reveals the one to one dependence $\delta P/P = -\delta f/f$. Given the precision of our breadboard design and the commercial tolerances of the mirrors, we are confident that the distortion is not due to a 5% focusing error. Furthermore, in the process of searching for the cause of the wavelength scale distortion, we observed that spectral

components in the decoder were dispersed at steeper angles relative to the encoders. The angle of incidence to the grating was well controlled by the breadboard design at $\alpha = 63.0$ degrees, and the observation wavelength was precisely controlled by a spatial mask placed at the encoder to create a sharp spectral feature at approximately 1532 nm. We measured a shift in dispersion angle of $\delta\beta = +0.76$ degrees from the expected angle of $\beta = 71.46$ degrees, or $\delta\beta/\beta = 1.06\%$. Taking a derivative of the plate factor P with respect to the dispersion angle β and using the grating equation, we find

$$\frac{\delta P}{P} = - \left(\frac{d}{\lambda} \sqrt{1 - ((\lambda/d) - \sin \alpha)^2} + \tan \beta \right) \delta \beta. \quad (2)$$

Evaluating this expression with the values already mentioned and $d = 833.33$ nm gives $\delta P/P = -0.0422$, which compares favorably with the observed value of a 5% distortion. The minus sign from the calculation is consistent with the fact that the measured spectrum shown in Fig. 5 occupies a wider spatial extent than desired, corresponding to a reduced plate factor P . The certainty in the value of the incident angle α and the observation wavelength leads us to examine the sensitivity of P to the groove spacing of the diffraction grating. A 5% distortion requires only $\delta d/d = -0.0023$! Thus, the observed distortion could result from a groove spacing of 831.41 nm instead of 833.33 nm or a groove density of 1202.7/mm versus 1200.0/mm. While the three holographic diffraction gratings used in the testbed were fabricated in the same batch, they were written independently and such small variations seem possible.

5 Improved Correlation Measurements

Having determined that the wavelength scale distortion can be a critical parameter in the correlation process, we conducted an experiment to correct the problem. While it is possible to increase the plate factor by increasing the incident angle α , which decreases β , this has the unwanted effect of *decreasing* the return angle of light from Mirror 1 while *increasing* the return angle from Mirror 2 (see Fig. 1). A simple alternative is to use a mask pattern at the decoder that compensates for the distortion. The pattern for super-code J_C was designed and fabricated with varying amounts of distortion (-2.5%, 0.0%, +2.5%, +5.0%, and +7.5%) to test the compensation. Shown in Fig. 8 is the autocorrelation signal measured with the original mask at the encoder and the intentionally distorted mask at the decoder. The received electrical signal is clearly maximized for the pattern with +5% distortion that matches the expansion of the spectral pattern. The measured autocorrelation power drops 29.4% going from a +5% to a zero distortion mask. The simulated autocorrelation curve for code J_C resembles Fig. 7 (a), with a more gradual reduction for increasing distortion. Because the code sequence for J_C has a number of repeated segments, a smaller proportion of light is directed to the wrong detector. The simulation predicted a 47.6% drop in autocorrelation power.

Measurements of improved crosscorrelation performance were less conclusive due to ambiguity in the horizontal position of the mask, as already discussed. For the decoder mask

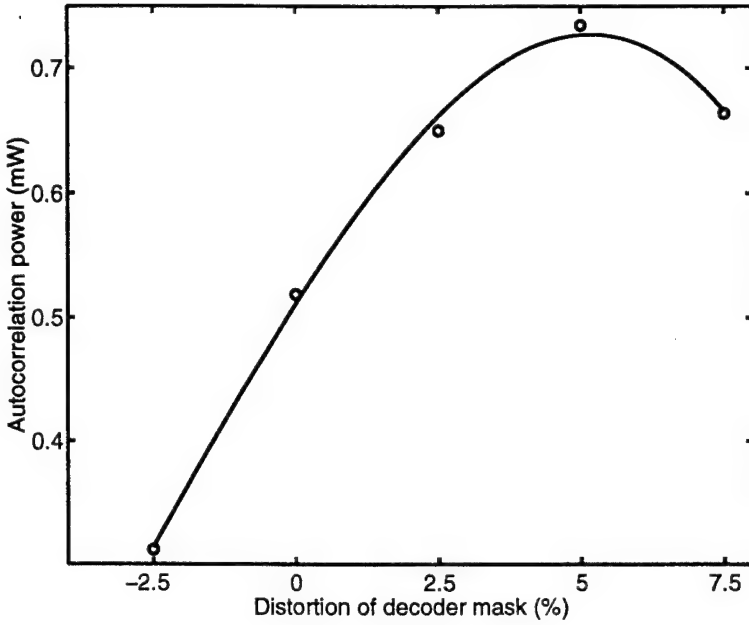


Figure 8: The autocorrelation signal measured on the spectrum analyzer as a function of the distortion of the mask pattern at the decoder. The data clearly shows that the signal is maximum at a +5% distortion, in agreement with the measured expansion of the received spectral pattern.

with distorted patterns, this problem was more pronounced because the spatial width of the patterns varies. As a result, it was possible to make adjustments during the measurements such that the crosscorrelation signal was on average 35 dB below the autocorrelation, regardless of the distortion of the decoder mask. Nevertheless, having demonstrated the improvement in autocorrelation performance that our simulation results suggest, we believe that similar improvements in crosscorrelation performance are also being achieved for code combinations with sensitivity to distortion.

6 Conclusion

Passive, all-optical correlators are attractive for high-speed network applications where asynchronous operation and independence of data rate are desired. They are able to process the extremely high combined data rate on a common network channel while the detection electronics operate at only individual user rates. However, the degradation of correlator performance has a direct impact on the capacity of a network to support simultaneously active users. Our numerical simulations, analytical results, and experimental measurements have identified wavelength scale distortion as a critical optical parameter in the correlation process and illustrated the importance of well-matched physical characteristics when using multiple gratings or other dispersive elements. Correlator designs that allow dynamic tuning, such as arrayed-waveguide devices featuring adjustable optical paths through temperature or mechanical tuning, might overcome this performance limitation. However, as the effects of

distortion are reduced, the impact of limited-resolution and other device specific effects will set a new, but lower limitation on correlator performance.

7 Acknowledgements

This work was jointly supported by the Texas Advanced Technology Program and the U.S. Air Force Office of Scientific Research. The authors wish to thank Dr. Marc D. Levenson for his expertise and experimental assistance.

References

- [1] J. Salehi, "Code division multiple-access techniques in optical fiber networks – part I: Fundamental principles," *IEEE Trans. Commun.*, vol. COM-37, pp. 824–833, Aug. 1989.
- [2] A. Weiner, J. Heritage, and J. Salehi, "Encoding and decoding of femtosecond pulses," *Optics Letters*, vol. 13, pp. 300–302, Apr. 1988.
- [3] M. Kavehrad and D. Zaccarin, "Optical code-division-multiplexed systems based on spectral encoding of noncoherent sources," *IEEE Journal of Lightwave Tech.*, vol. LT-13, pp. 534–545, Mar. 1995.
- [4] L. Nguyen, B. Aazhang, and J. F. Young, "All-optical CDMA with bipolar codes," *Electron. Lett.*, vol. 31, pp. 469–470, Mar. 1995.
- [5] L. Nguyen, T. Dennis, B. Aazhang, and J. F. Young, "Experimental demonstration of bipolar codes for optical spectral amplitude CDMA communication," *IEEE Journal of Lightwave Tech.*, in press, Sept. 1997.

Imaging characteristics of poly(methyl methacrylate) at vacuum ultraviolet wavelengths

I. E. Ferincz,^{a)} Cs. Tóth,^{b)} and J. F. Young^{c)}

Department of Electrical and Computer Engineering and the Rice Quantum Institute, Rice University, Houston, Texas 77251

(Received 11 October 1996; accepted 9 May 1997)

We report the depth versus exposure characteristics of poly(methyl methacrylate) (PMMA) in the vacuum ultraviolet (VUV) region from 59 to 128 nm. Calculated absorption coefficients of the PMMA are also presented. The depth of the features on the PMMA were in the range of 20–80 nm created by 1–50 mJ cm⁻² exposures and were measured with an atomic force microscope (AFM). We found that the AFM can reliably measure depth differences of only 2 nm. The sensitivity of the AFM permits exposures to be reduced for high resolution microscopy and holography even in the case of highly absorbing films. © 1997 American Vacuum Society. [S0734-211X(97)12404-0]

I. INTRODUCTION

Microscopy using contact printing or holography requires a well characterized, high resolution recording film. One of the earliest and best characterized electron and x-ray resists is poly(methyl methacrylate) (PMMA).^{1–3} In contrast, however, to lithography applications — where the full removal of the resist is desirable in the exposed areas — contact imaging and holography require a resist with vertical (depth) resolution. The attainability of a “grey-scale” pattern in the resist is important in these applications for reliable and reproducible mapping of the light intensity in a wide exposure range. In the soft x-ray region, microscopy using PMMA as a resist material is well developed.⁴ In PMMA, a positive resist, bonds are broken by incident short wavelength radiation, decreasing the average molecular weight of the long-chain molecules. This increases the solubility of the resist in a suitable solvent, resulting in a pattern of surface heights corresponding to the exposure. The surface pattern can be measured by a scanning⁵ or transmission electron microscope,^{6,7} but an atomic force microscope (AFM) provides more reliable quantitative data.^{8,9}

Vacuum ultraviolet (VUV) microscopy has the potential to supplement x-ray and electron microscopy, because the contrast mechanism is quite different. VUV radiation interacts with the outer valence electrons and molecular absorption is sensitive to composition and structure. In addition, several reasonably practical incoherent and coherent sources exist in the 80–130 nm region. However, almost no studies have been made of PMMA, or other films, for VUV imaging. While there are lithography studies in the 110–260 nm region,^{10–12} this information is only partly relevant since the requirements of lithography are quite different from imaging. For lithography, the critical parameter is the exposure required to completely remove the film; imaging, however, requires quantitative knowledge of the response function and

a reasonable dynamic range, or intensity level resolution. The relationship between exposure and surface height is generally poorly known even for common photoresists. Basic and important optical constants, such as absorption coefficient at VUV wavelengths are also lacking.

In this work we will present the depth-exposure characteristics of PMMA in the 59–128 nm spectral range, for exposure values of 1–50 mJ cm⁻². The surface depths were measured with an AFM and were in the range of 2–80 nm. Since the AFM can reliably measure surface height differences of only 2 nm, very low exposures can be used even at wavelengths that are highly absorbing. We have used our depth versus exposure data to calculate the VUV absorption coefficients of PMMA using a simple model for exposure and dissolution.

II. EXPERIMENTAL DESCRIPTION

A. Preparation and development of the PMMA resist

The samples for exposure were 12.5 mm diameter polished glass disks spin coated with PMMA. The resist was a commercial solution of 4% PMMA (molecular weight of 950 000) in chlorobenzene.¹³ The top surface of the substrate was flooded with the PMMA solution and then spun at 5000 rpm for 25 s. A second layer of PMMA was spun over the first to provide a thicker film. The resulting film was 290±10 nm thick as measured by the AFM. The substrate and film was then baked at 140 °C for at least 30 min in a vacuum oven at ~500 mbar pressure.

Following exposure the film was developed in pure methyl isobutyl ketone for 60 s at 25±0.5 °C, during which time the developer was agitated mildly. Following development, the sample was immediately rinsed in isopropyl alcohol for 5 s, dried with a jet of clean freon, and baked again at 140 °C for 30 min.

B. System setup

Figure 1 shows the experimental arrangement. Broadband incoherent VUV light was generated using a laser-produced plasma. Pulses from a *Q*-switched Nd:YAG laser were fo-

^{a)}Present address: Department of Optics and Quantum Electronics, JATE University, H-6720 Szeged, Dóm tér 9, Hungary.

^{b)}Permanent address: Research Institute for Solid State Physics, P.O. Box 49, H-1525, Budapest, Hungary.

^{c)}Electronic mail: young@rice.edu

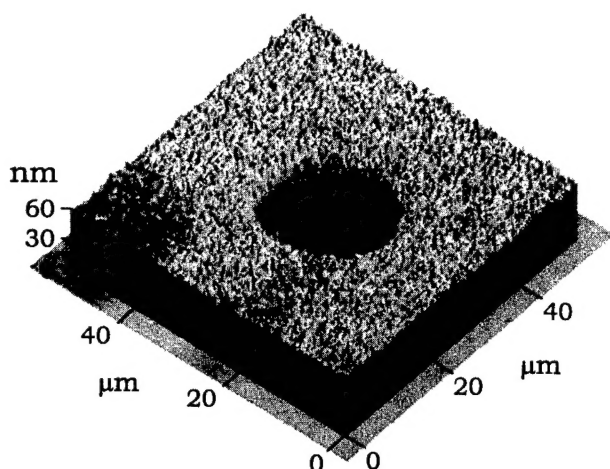


FIG. 4. An atomic force micrograph of a contact printed pattern on the surface of PMMA.

exposure was obtained by simply multiplying this average exposure value per laser pulse by the total number of pulses in an exposure.

In order to account for possible long-term changes in the efficiency of the laser-produced plasma and the light collection system, we interrupted each exposure to take source spectra at Port No. 2. The number of spectra taken was varied to achieve good average values. Three spectra were measured for the shortest (3 and 4 min) exposures and seven for the longest (60 min) exposures. The exposure energy was calculated by averaging the spectra.

D. Depth measurement by AFM

The transverse and vertical scans of the AFM¹⁶ were calibrated using a calibration grating and height standards. A typical atomic force micrograph of a contact printed test pattern on the surface of the PMMA is shown in Fig. 4. To obtain a good estimate of the depth of a given hole, four $\sim 50 \times 50 \mu\text{m}$ (256 by 256 pixels) scans were made using different scanning directions and the results averaged. Typically, the standard deviation of the pixel height from the average was $\sim 3 \text{ nm}$. However, because of the large number of pixels, this deviation did not effect the depth measurement directly, since the *average* height of the pixels were compared. However, this high frequency noise did introduce errors during the removal of the apparent surface curvature. Apparent surface curvature is an inherent byproduct of the AFM transverse scanning mechanism, and it can be well approximated by a second order polynomial. The elimination of the curvature was performed by fitting a second order polynomial to each data row of the scans. The accuracy of this fit is reduced by the pixel height variation because of the small number of pixels in each row. This was particularly true where the data row contained values from both the exposed and unexposed parts, since the unexposed part was not included in the fitting. We estimate that the vertical resolution was limited to 2 nm by this effect.

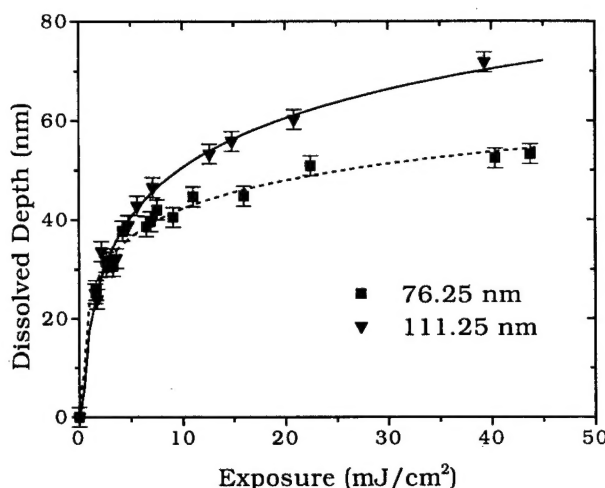


FIG. 5. Developed film depth vs exposure for PMMA at two different wavelengths. The symbols with error bars are the measured height differences between exposed and unexposed regions, while the lines are the results of a model fitted to the data.

III. RESULTS AND DISCUSSION

Measurement of exposure patterns such as Fig. 4 resulted in characteristic curves of depth versus exposure, S , at specific wavelengths spaced 4.25 nm over the range of 59–128 nm. Figure 5 shows two such curves; the symbols represent measured data while the lines are the result of the exposure-dissolution model discussed below. This set of curves can be usefully summarized by defining a specific exposure flux, S_p , for each wavelength that will produce a 30 nm deep pattern. Figure 6 shows a plot of S_p over the wavelength range measured. While the 30 nm criteria is arbitrary, we found that patterns of this depth resulted in low noise, reproducible measurements. Also shown in Fig. 6 is the calculated derivative of pattern depth versus exposure, $G = dz/dS$, evaluated at S_p . The parameter G is a measure of the exposure resolution; a large G indicates there are more distinguishable intensity levels within a given exposure range.

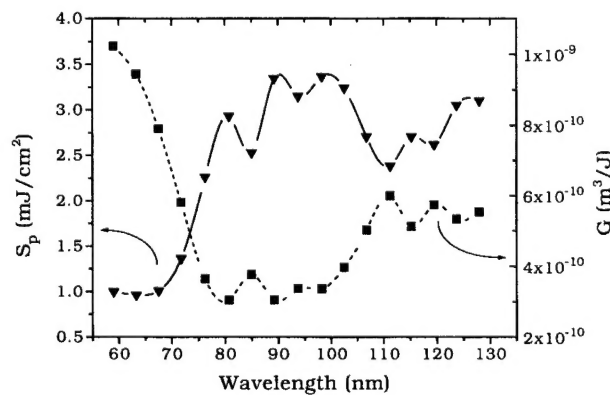


FIG. 6. Specific exposure S_p required for a developed depth of 30 nm, (triangles), as a function of wavelength, and G , the derivative of depth with respect to exposure at S_p , (filled squares), characterizing the possible grey-scale levels for imaging applications.

reconstruction of contact and holographic recordings. We found that exposures as small as 2 mJ cm^{-2} can produce patterns 20 nm deep. Since the AFM can resolve ~ 2 nm depth differences, about ten vertical or exposure levels are distinguishable. This exposure level is significantly lower than that previously used with other depth measurement techniques.^{1,5} Further improvement should be possible by decreasing the pixel noise, perhaps by modifying the film preparation and developing procedures.

ACKNOWLEDGMENTS

This work was jointly supported by the National Science Foundation, and the U.S. Air Force Office of Scientific Research.

¹G. D. Kubiak *et al.*, in *OSA Proceedings on Soft-X-Ray Lithography*, edited by J. Bokor (Optical Society of America, Washington, DC, 1991), Vol. 12, pp. 124–128.

²R. J. Hawryluk, H. I. Smith, A. Soares, and A. M. Hawryluk, *J. Appl. Phys.* **46**, 2528 (1975).

³J. S. Greeneich, *J. Electrochem. Soc. Solid State Sci. Technol.* **122**, 970 (1975).

⁴X-Ray Microscopy III, edited by A. G. Michette, G. R. Morrison, and C. J. Buckley (Springer, Berlin, 1992).

⁵G. C. Bjorklund, S. E. Harris, and J. F. Young, *Appl. Phys. Lett.* **25**, 451 (1974).

⁶M. Howells *et al.*, *Science* **238**, 514 (1987).

⁷K. Shinohara, A. Ito, and Y. Kinjo, in *Applications of Laser Plasma Radiation* (SPIE, Bellingham, WA, 1994), Vol. 2015, pp. 10–19.

⁸R. A. Cotton *et al.*, in *Applications of Laser Plasma Radiation* (SPIE, Bellingham, WA, 1994), Vol. 2015, pp. 86–96.

⁹A. D. Stead, A. M. Page, and T. W. Ford, in *Applications of Laser Plasma Radiation II* (SPIE, Bellingham, WA, 1995), Vol. 2523, pp. 40–50.

¹⁰K. Kudo *et al.*, *Jpn. J. Appl. Phys.* **1** **29**, 2572 (1990).

¹¹K. Kudo *et al.*, *Jpn. J. Appl. Phys.* **1** **31**, 401 (1992).

¹²J. C. White *et al.*, *Appl. Phys. Lett.* **44**, 22 (1984).

¹³PMMA 950K Resist in Chlorobenzene, Cat. No. 897631, OCG Microelectronics, 3 Garret Mountain Plaza, West Paterson, NJ 07424.

¹⁴Picomotor, New Focus, Inc., 2630 Walsh Avenue, Santa Clara, CA 95051.

¹⁵J. A. Samson, *Techniques of Vacuum Ultraviolet Spectroscopy*, 2nd ed. (Pied, Lincoln, NE, 1980).

¹⁶AutoProbe Microscope System, Park Scientific Instruments, 1171 Borregas Ave., Sunnyvale, CA 94089.

¹⁷G. H. Bernstein, D. A. Hill, and W. Liu, *J. Appl. Phys.* **71**, 4066 (1992).